

Single-neutron knockout from intermediate energy beams of $^{30,32}\text{Mg}$: Mapping the transition into the “island of inversion”

J. R. Terry, B. A. Brown, C. M. Campbell, J. M. Cook, A. D. Davies, D.-C. Dinca, A. Gade, T. Glasmacher, P. G. Hansen, B. M. Sherrill, and H. Zwahlen

*National Superconducting Cyclotron Laboratory, Michigan State University, East Lansing, Michigan 48824, USA and
Department of Physics and Astronomy, Michigan State University, East Lansing, Michigan 48824, USA*

D. Bazin and K. Yoneda

National Superconducting Cyclotron Laboratory, Michigan State University, East Lansing, Michigan 48824, USA

J. A. Tostevin

Faculty of Engineering and Physical Sciences, University of Surrey, Guildford GU2 7XH, United Kingdom

T. Otsuka

*Department of Physics and Center for Nuclear Study, University of Tokyo, Hongo, Tokyo 113-0033, Japan and
RIKEN, Hirosawa, Wako-shi, Saitama 351-0198, Japan*

Y. Utsuno

Advanced Science Research Center, Japan Atomic Energy Agency, Tokai, Ibaraki 319-1195, Japan

B. Pritychenko

Brookhaven National Laboratory, Upton, New York 11973-5000, USA

(Received 5 March 2007; revised manuscript received 15 October 2007; published 29 January 2008)

The breakdown of the $N = 20$ magic number in the so-called island of inversion around ^{32}Mg is well established. Recently developed large-scale shell-model calculations suggest a transitional region between normal- and intruder-dominated nuclear ground states, thus modifying the boundary of the island of inversion. In particular, a dramatic change in single-particle structure is predicted between the ground states of ^{30}Mg and ^{32}Mg , with the latter consisting nearly purely of $2p\text{-}2h$ $N = 20$ cross-shell configurations. Single-neutron knockout experiments on $^{30,32}\text{Mg}$ projectiles have been performed. We report on a first direct observation of intruder configurations in the ground states of these very neutron-rich nuclei. Spectroscopic factors to low-lying negative-parity states in the knockout residues are deduced and compare well with shell-model predictions.

DOI: [10.1103/PhysRevC.77.014316](https://doi.org/10.1103/PhysRevC.77.014316)

PACS number(s): 21.10.Jx, 21.60.Cs, 25.70.Hi, 27.30.+t

I. INTRODUCTION

A disappearance of the $N = 20$ magic structure in neutron-rich nuclei was first suggested based on the mass measurement of ^{31}Na [1]. Subsequent observations revealed a region of deformation around the $N = 20$ isotones with $Z \leq 12$ [2–9]. Shell-model calculations performed for a broad range of nuclei in this vicinity indicate that two-particle-two-hole ($2p\text{-}2h$) configurations across the $N = 20$ shell gap are lower in energy than normal configurations for nuclei with $20 \leq N \leq 22$ and $10 \leq Z \leq 12$, illustrated in Fig. 1. This region of nuclei, referred to as the “island of inversion” [10], represents a dramatic change of structure with growing proton-neutron asymmetry and has attracted much attention from both experiment and theory. Most notably, recent efforts have concentrated on the boundary of this region, which observations characterize as a transitional region [11–14] as opposed to a hard border as was originally suggested in Ref. [10].

The $N = 20$ island of inversion around ^{31}Na provides an important benchmark for the understanding of mechanisms that give rise to dramatic changes in single-particle structure and deformation in exotic nuclei. Although islands of inversion

exist or are expected to exist in other regions of the nuclear landscape [15], the $N = 20$ island lies in a mass region in which effective interactions can be developed with high predictive power. As opposed to the region around ^{12}Be in which an inversion is also observed [16,17] and effective interactions are also quite accurate, the nuclear landscape around ^{32}Mg is more extended, allowing a systematic investigation of changes in single-particle structure.

Weakening of the $N = 20$ shell gap has been suggested in Refs. [18,19] as a consequence of the spin-isospin interaction. Such a reduced gap poses a formidable task for nuclear shell-model calculations. The importance of $np\text{-}nh$ configurations across the $N = 20$ gap requires model spaces that include both sd and fp single-particle states. Truncation schemes are necessary to reduce the dimension of the effective Hamiltonian matrix to a manageable size. Effective interactions have been developed in which the configuration space is limited to $0p\text{-}0h$ and $2p\text{-}2h$ neutron cross-shell configurations. However, the possible pitfalls of such a truncation are discussed in Ref. [10]. The recent Monte Carlo shell-model (MCSM) approach offers a framework in which much larger model spaces can be

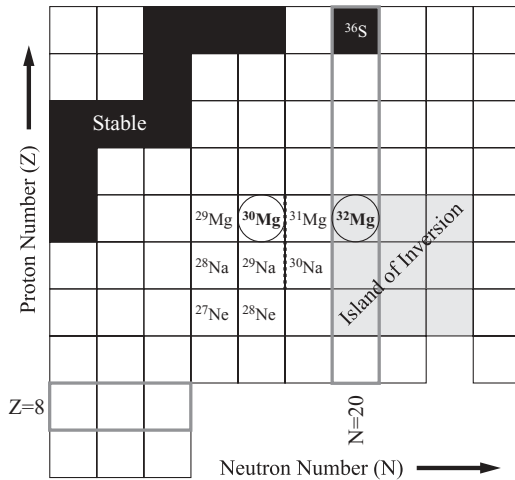


FIG. 1. Chart of nuclides around the island of inversion. Stable nuclei are shown in black and the island of inversion as discussed in Ref. [10] is shown in gray. The isotopes investigated in the present work are circled. The heavy dotted line represents the recently observed transition from normal-dominated to intruder-dominated ground states in the magnesium and sodium chains. This transition is not yet clearly delineated for the neon isotopes.

accommodated and unrestricted mixing of np - nh configurations is allowed [18,20].

The SDPF-M effective interaction, developed with the MCSM approach, includes the $0d_{5/2}$, $1s_{1/2}$, $0d_{3/2}$, $0f_{7/2}$, and $1p_{3/2}$ single-particle states [21]. SDPF-M calculations have been shown to accurately model sd nuclei [21], i.e., nuclei that have previously been well represented by effective interactions that only include sd single-particle states (the USD interaction [22]). Further, the SDPF-M interaction has proven to be accurate in describing the onset of deformation in the island of inversion and provides a theoretical treatment of the transitional region from ground states dominated by normal configurations to those dominated by $N = 20$ cross-shell intruder configurations [23].

The SDPF-M predictions of two-neutron separation energies, $E(2_1^+)$, and $B(E2; 2_1^+ \rightarrow 0_1^+)$ excitation strength for a number of nuclei in this region are found to be in agreement with experimental values [24]. It is noted that, as opposed to a definite boundary, SDPF-M calculations suggest a transitional region into the island of inversion [24]. For $N > 17$, a growing amount of empirical evidence has been deduced in support of this transition from normal to intruder dominance for magnesium and sodium isotopes. Although ^{30}Mg ($N = 18$) is well described without considering cross-shell configurations [5,25] indicating negligible intruder content in the ground state, at $N = 19$ the low-energy level structure [26,27] and the recently measured magnetic moment of its ground state [11] indicate a strong admixture of intruder configurations in ^{31}Mg . Therefore, for $Z = 12$ isotopes there appears to be a sharp transition at $N = 19$ into the island of inversion. For sodium with just one proton less, recent systematic calculations [23], which agree with measured observables for this isotopic chain, suggest a more gradual transition. The $N = 19$ nuclide ^{30}Na is concluded to lie within the island of inversion [23], whereas measurements for ^{29}Na , predicted to be outside of the island,

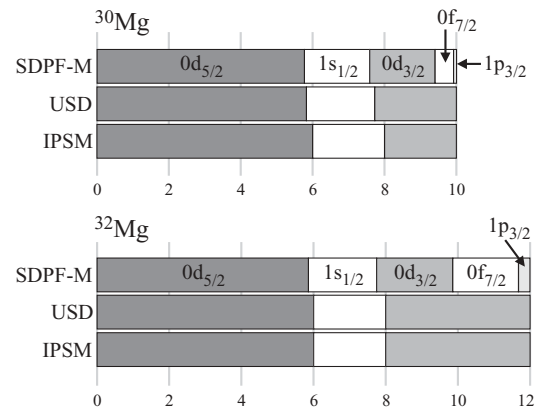


FIG. 2. Calculated neutron single-particle occupancies. Neutron single-particle occupancies calculated using the USD interaction and the SDPF-M interaction are compared. The independent particle shell model (IPSM) represents normal filling.

indicate a significant intruder admixture [12]. Sufficient data do not exist to systematically track the transition in the neon isotopic chain. However, already at $N = 18$, ^{28}Ne shows characteristics indicating that it is on the boundary of the island of inversion [5,28], and for ^{27}Ne , intruder states have been observed at low excitation energy [13,29,30].

In the present measurement the single-particle structures of the $^{30,32}\text{Mg}$ ground states are probed by single-neutron knockout at intermediate beam energy. SDPF-M calculations predict a dramatic change in the single-particle structure of these nuclei. Whereas the SDPF-M ^{30}Mg ground state wave function is dominated by normal configurations with an occupancy of only 0.6 neutrons in fp single-particle states, the ^{32}Mg ground-state wave function is a nearly pure $2p$ - $2h$ configuration across the $N = 20$ shell gap with a neutron fp occupancy of 2.15. This shift in structure is illustrated in Fig. 2. In this figure, SDPF-M predicted neutron single-particle occupancies are compared to Universal SD (USD) and independent-particle shell-model (IPSM) predictions. The USD effective interaction includes only sd single-particle states in its model space and, therefore, does not allow for $N = 20$ shell-breaking effects [22]. The IPSM results represent normal filling of single-particle states. For both ^{30}Mg and ^{32}Mg , the $0d_{5/2}$ and $1s_{1/2}$ occupancies from all three models are in good agreement. The most significant differences are observed in the $0d_{3/2}$ and fp orbits. Comparisons of the $0d_{3/2}$ occupancies from the USD and SDPF-M interaction reveal that a small fraction of the $0d_{3/2}$ neutrons are promoted to fp orbits when shell-breaking effects are included. This effect is also observed in ^{32}Mg but with a much larger fraction promoted. In effect, the two additional neutrons added to ^{30}Mg occupy single-particle states in the fp shell as opposed to filling the remaining sd space.

Nucleon knockout experiments in inverse kinematics are sensitive to the occupation number of single-particle orbitals [31,32] and represent a selective spectroscopic tool to investigate the evolution of shell closures in rare isotopes. This method allows for detailed spectroscopy of the ground-state wave function of the projectile and can provide a quantitative measure of intruder content. Intruder configurations are

observed in this direct reaction through the measurement of significant spectroscopic strength to states in the reaction product with the parity of the intruding shell. Further, the single-particle strength quantifies the extent of the admixture of intruder configurations in the ground state of the projectile.

Observables in the present measurements include partial knockout cross sections to individual final states and longitudinal momentum distributions of the mass $A-1$ knockout fragments. These observables are modeled in a three-body reaction calculation based on the eikonal and sudden approximations and making use of Glauber theory [33,34]. Whereas the partial cross sections are sensitive to the single-particle structure of the wave function of the projectile, the longitudinal momentum distributions are sensitive to the orbital angular momentum quantum number ℓ of the knocked-out nucleon, providing spectroscopic information as well [35–37].

II. EXPERIMENT

The experiment was performed at the National Superconducting Cyclotron Laboratory on the campus of Michigan State University. Radioactive ion beams of ^{30}Mg and ^{32}Mg , also called secondary beams, were produced by fragmentation at the Coupled-Cyclotron Facility [38] and filtered in the A1900 fragment separator [39]. Specifics of the secondary beam production process are listed in Table I.

The secondary beams impinged on a 376(4) mg/cm² beryllium reaction target located at the target position of the S800 spectrograph [40]. Data for particle identification, by means of an energy loss versus time-of-flight method, and for event-by-event momentum reconstruction are collected using the S800 focal plane detector setup [41]. The segmented germanium array (SeGA) [42] was positioned around the reaction target to tag individual excited states populated in the reaction by detection of γ radiation coincident with knockout residues.

SeGA is an array of 18 32-fold segmented high-purity germanium detectors designed for in-beam γ -ray spectroscopy at fragmentation energies. The array was arranged in the δ configuration consisting of nine angle pairs at 24°, 29°, 40°, 60°, 78°, 90°, 126°, 139°, and 147° with respect to the beam axis. The response of the array is characterized by a 2.4% photopeak efficiency for 1.0 MeV γ -rays emitted from

TABLE I. Summary of radioactive ion beam production for the $^{30,32}\text{Mg}$ secondary beams. The bottom row lists the momentum spread ($\Delta P/P$) of the secondary beams. The energy at the center of the reaction target (at the S800 target position) is listed as the secondary beam energy.

	^{30}Mg	^{32}Mg
Primary beam	^{40}Ar	^{48}Ca
Production target	140 MeV/nuc.	140 MeV/nuc.
Sec. beam energy	^9Be	^9Be
$\Delta P/P$	611 mg/cm ²	775 mg/cm ²
	85.8(15) MeV/nuc.	75.7(13) MeV/nuc.
	1%	2%

a stationary source and a 3% energy resolution for 1.0 MeV γ -rays emitted in-flight from a source with $v/c \approx 0.4$.

To maximize the secondary beam intensity, the spectrograph optics were set to focus the secondary beam on the reaction target. The longitudinal momentum of the knockout fragments is corrected on an event-by-event basis for the momentum of the projectile, measured at the intermediate image of the S800 analysis line [40]. Resolutions of 45 and 50 MeV/ c full width at half maximum (FWHM), or 0.38% and 0.43%, were obtained for the ^{30}Mg and ^{32}Mg secondary beams.

III. ANALYSIS AND EXPERIMENT RESULTS

A. Single-neutron knockout from ^{30}Mg

The inclusive single-neutron knockout cross section from ^{30}Mg to ^{29}Mg is determined to be 100(2) mb. Leading sources of uncertainty are the S800 acceptance (1%), software cuts for particle identification (1%), the PID detector efficiencies (1%), and the target thickness (1%). This inclusive cross section includes acceptance corrections within the acceptance of the S800 but not corrections based on extrapolation beyond the acceptance.

The Doppler-reconstructed γ -ray energy spectrum in coincidence with ^{29}Mg fragments is shown in Fig. 3. Nine photopeaks are clearly observed in the spectrum as indicated in the figure. The peak at 0.3 MeV is found to be much broader than the expected 15-keV FWHM for a photopeak at this

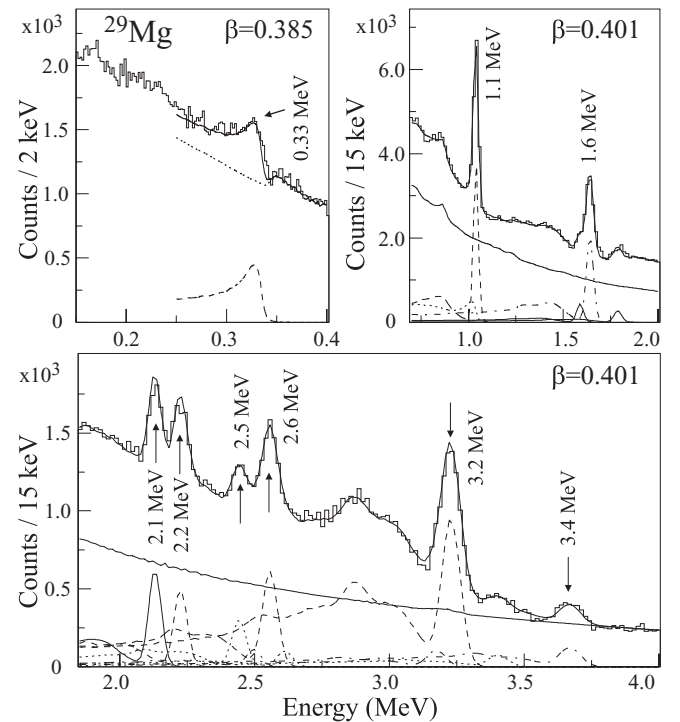


FIG. 3. Gamma-ray spectrum in coincidence with ^{29}Mg fragments. The upper-right panel shows the low-energy region of the spectrum that is Doppler reconstructed using the post-target fragment velocity. The midtarget velocity is used in the Doppler reconstruction of the remainder of the spectrum. Results of a χ^2 fit to the low-energy region and to the 0.5- to 4.0-MeV region are overlaid.

energy. This suggests that the emitting state has a relatively long lifetime. Therefore, the low-energy region of the spectrum is Doppler reconstructed with the post-target fragment velocity of $0.385c$ as the majority of these γ -rays are emitted after the fragment has left the target. The angle for the Doppler reconstruction is still calculated assuming emission from the center of the target, giving rise to the low-energy tail. The remainder of the γ -ray spectrum, above 0.5 MeV, is Doppler reconstructed using the midtarget fragment velocity of $0.401c$. The post-target velocity is calculated from the fragment momentum measured in the S800 focal plane, whereas the midtarget velocity is determined in two ways that give consistent results: (1) an energy loss calculation through half of the reaction target using ATIMA [43,44] within the LISE++ program [45] and the fragment momentum measured in the S800 and (2) an iterative Doppler reconstruction procedure in which the reaction target position and the midtarget velocity are adjusted to align the 1.040-MeV transition at the known energy for all detection angles.

γ -ray intensities are obtained through χ^2 fits of calculated response functions to the Doppler-reconstructed spectrum. The response of the array to a transition γ -ray is calculated in a GEANT3 simulation. A dead layer of germanium is included along the outer circumference of the cylindrical crystal in the simulation with a thickness adjusted to match the measured photopeak efficiency from calibration data. The simulated full response function for a 1.332-MeV γ -ray, which includes the photopeak, Compton continuum, and escape and annihilation peaks, deviates by no more than 10% from observations from a stationary ^{60}Co source. The simulated photopeak efficiency deviates by no more than 5% from measured values obtained with stationary sources from 0.25 MeV up to 3.2 MeV. Input parameters for the simulation include the γ -ray energy, the half-life of the emitting state, and the fragment velocity along with the target position and fragment velocity assumed in the Doppler reconstruction.

γ -ray intensities in the region between 0.7 and 4.0 MeV are taken from a single fit to the spectrum that includes simulated response functions for each transition γ -ray and a continuum γ -ray distribution. The shape of the continuum is fixed for energies above 1 MeV using data from a $^9\text{Be}(^{28}\text{Ne},^{27}\text{Ne})\text{X}$ reaction [13] and from the $^9\text{Be}(^{32}\text{Mg},^{31}\text{Mg})\text{X}$ data presented in the present article. No transition γ -rays are observed in coincidence with these reactions above 1 and 2.5 MeV, respectively. As the background observed for the ^{27}Ne and ^{31}Mg fragments does not extrapolate well below 1 MeV, a free varying exponential is also included, which gives a negligible contribution above 1 MeV after χ^2 minimization.

The fit to the spectrum between 0.7 to 4.0 MeV includes simulated photopeaks for seven known transitions within this region of the spectrum that are clearly observed in the present measurement: 1.04, 1.64, 2.13, 2.21, 2.45, 2.56, and 3.23 MeV [46,47]. After an initial χ^2 minimization, five simulated photopeaks corresponding to previously observed transitions are added where inclusion would clearly reduce significant fluctuations in the fit residual. Two previously unobserved transitions are added at 1.79 and 3.41 MeV. Although the statistics are limited for these low-intensity photopeaks, both seem to appear in Doppler-reconstructed spectra from the

forward (24° , 29° , 40°), middle (60° , 78° , 90°), and backward (126° , 139° , 147°) groups of angle-pairs, suggesting that these γ -rays are emitted from the fast-moving projectile-like residue. The fit also includes energy offsets for a few response functions that do not align well with photopeaks in the data. With the exception of the 2.21 MeV peak which requires a shift in energy of +17 keV to fit the spectrum, no other significant offsets are found. Given the large offset required for the 2.21 MeV peak, this peak is not associated with any previously observed transition.

To accurately deduce the intensity of the 0.336 MeV photopeak the long half-life of the emitting state must be included in the simulation of the response function. Because the half-life of the 1.431 MeV state is not known, response functions for several assumed half-lives are generated and fit to the data. In addition to the calculated response function, the fit includes a γ -ray background and a Doppler-smear annihilation peak. The γ -ray background in this energy region is dominated by backscattering, and the shape is estimated by analysis of the γ -ray energy spectrum in coincidence with ^{28}Mg fragments, which was collected simultaneously with the ^{29}Mg fragments and shows no photopeaks below 1.5 MeV. The 0.511-MeV annihilation peak observed at forward angles is broadened and shifted to approximately 0.35 MeV by the Doppler reconstruction. This distorted peak is simulated and then scaled to match the intensity of the 0.511-MeV photopeak in the forward-angle lab-frame energy spectrum. So the fit to the ^{29}Mg γ -ray energy spectrum includes four parameters: the half-life of the emitting state, the intensity and position of the photopeak in the response function, and the scale of the background.

A contour plot of the χ^2 as a function of the half-life and intensity associated with the 0.336-MeV photopeak is shown in Fig. 4. For each point in this two-dimensional space, the

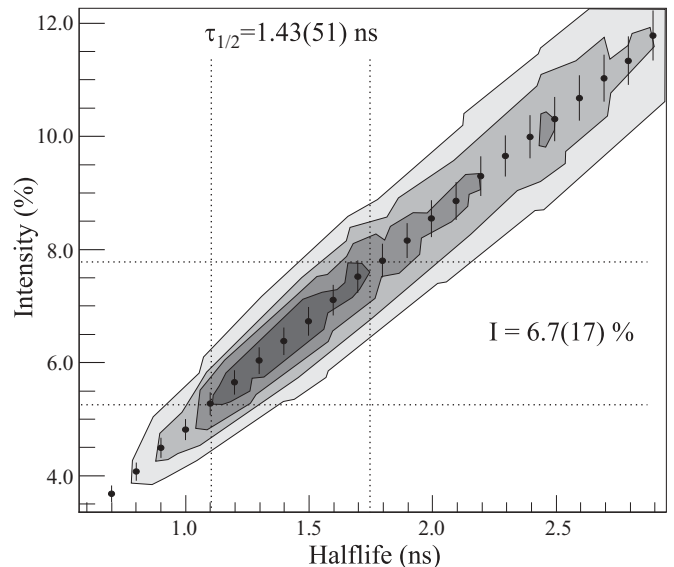


FIG. 4. Analysis of ^{29}Mg 0.336-MeV photopeak. The one-, two-, three-, and four- σ contours are shown illustrating confidence intervals for the simultaneous fit of both intensity and half-life associated with the 0.336-MeV photopeak.

χ^2 is minimized with respect to the remaining two parameters. A clear correlation between the half-life and intensity is observed, and the contours represent one-, two-, three-, and four- σ limits for the uncertainty in the deduced values for these parameters. The half-life is found to be 1.43(51) ns, whereas the intensity is 6.7(17)%, relative to the total single-neutron knockout cross section. In addition to the statistical uncertainties reflected in Fig. 4, a systematic uncertainty of 5% and 0.2 ns for the respective intensity and half-life are included, arising from the matching of the simulation to measured photopeak detection efficiencies. Because this experiment was not designed for precision lifetime measurements and better measurements will likely become available, the figure also includes, for future use, data points with statistical uncertainties representing the deduced intensity assuming a fixed half-life. An additional 5% systematic uncertainty must be added to these data points as well.

Figure 4 reveals a local minimum at 2.5 ns just inside the 2σ contour. This minimum and the one at 1.43 ns are separated by $\Delta\chi^2 = 6$. However, if the slope of the background is flattened by 5%, the minimum at 2.5 ns falls just below the one at 1.43 ns. The half-life of the state at 1.431 MeV is concluded to be 1.43(51) ns with 1σ uncertainty quoted and no systematic uncertainty in the shape of the background included. A precision measurement of the lifetime of this state would be helpful in reducing the uncertainty in the present results.

Results of the γ -ray analysis for the ^{29}Mg fragment are shown in Table II. Intensities are taken from the fit to the γ -ray spectrum and are normalized on the number of reactions, deduced by simultaneous measurement of the number of ^{29}Mg fragments. Branching ratios are deduced by intensity balancing. The three previously unobserved transitions are not included in the intensity balancing as their placement is not known. However, it is noted that the 1.79-MeV transition,

TABLE II. Gamma-ray intensities and branching ratios for ^{29}Mg .

E_{level} (MeV)	E_{γ} (MeV)	I (%)	b (%)	σ (mb)	ℓ
0.000			47.4(36)	47.4(38)	
0.055					
1.095	1.040	8.5(11)	4.3(15)	4.3(15)	1
1.431	0.336	6.7(17)	6.7(17)	6.7(17)	3
1.642	1.642	9.0(11)	7.3(15)	7.3(15)	
2.500	2.445	2.7(10)	3.7(14)	3.7(15)	(2,3)
	2.500	1.0(10)			
2.615	2.560	5.9(11)	6.9(15)	6.9(15)	(0,1)
	2.615	1.0(10)			
3.232	1.586	1.8(10)	21.5(22)	21.5(22)	2
	2.133	4.3(10)			
	3.178	1.5(11)			
	3.232	13.9(13)			
3.674	3.674	2.3(10)	2.3(10)	2.3(10)	
	1.79(1)	1.4(10)			
	2.23(1)	3.7(10)	Unplaced transitions		
	3.41(1)	1.2(10)			

based on its energy alone, is a candidate for a transition between the doublet at 3.23 MeV and the state at 1.431 MeV. The partial cross sections are deduced by multiplication of the extracted branching ratios by the inclusive cross section of 100(2) mb. The rightmost column in Table II lists deduced angular-momentum quantum numbers ℓ for the removed nucleon based on analysis of longitudinal momentum distributions discussed below.

Longitudinal momentum distributions are extracted by gating on the 0.336- and 1.040-MeV photopeaks and the 3.23-MeV doublet photopeak. Contributions to the distributions from the γ -ray background are estimated by applying energy gates just above these peaks in the spectrum. Background contributions are subtracted to yield the distributions shown in Fig. 5. Acceptance corrections are determined in a Monte Carlo calculation in which particles are tracked through the known geometry and optics of the spectrograph using the COSY infinity transport code [48]. Each plot is overlaid with calculated distributions assuming a number of ℓ values for the knocked-out nucleon. The 3.23-MeV doublet shows a clear $\ell = 2$ character, whereas the 1.040-MeV distribution suggests $\ell = 1$ for this state. The overlaid distributions for

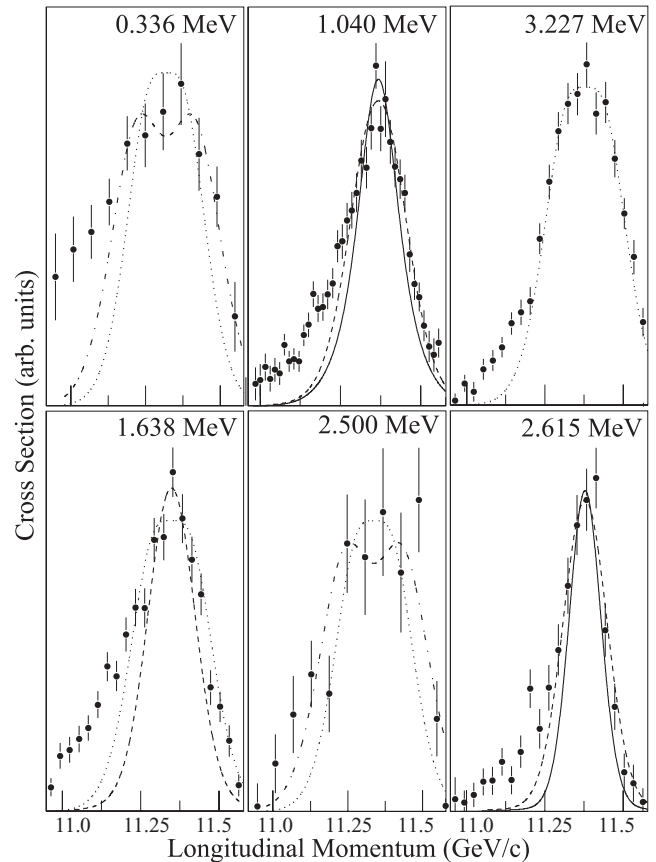


FIG. 5. Longitudinal momentum distribution for states populated in the knockout fragment ^{29}Mg . The corresponding γ -ray energy gate is given at the top of each panel, and calculated distributions assuming $\ell = 0$ (solid), $\ell = 1$ (dashed), $\ell = 2$ (dotted), and $\ell = 3$ (dot-dashed) are overlaid. Both $\ell = 0$ and $\ell = 1$ calculations for the 1.040 distribution include a 50% $\ell = 2$ contribution to account for observed indirect feeding.

the 1.040-MeV state include a 50% contribution by area of $\ell = 2$ to account for the observed indirect feeding from the 3.23-MeV doublet. The 0.336-MeV distribution is very broad and consistent with an $\ell = 3$ assignment.

The distribution associated with direct population of the state at 1.638 MeV, shown in Fig. 5, is consistent with an $\ell = 2$ assignment. However, the distribution may be better modeled by a combination of $\ell = 2$ and a narrower distribution of either $\ell = 0$ or $\ell = 1$, suggesting the possibility of unobserved indirect feeding to this state. Distributions are also extracted for direct population of the states at 2.500 and 2.615 MeV, but, given the complexity of the γ -ray spectrum and the lower intensity of these photopeaks, subtraction of contributions from the background and nearby photopeaks leads to significant statistical and systematic uncertainties. The distribution for the state at 2.500 MeV appears broad, suggesting an assignment of $\ell = 2, 3$, whereas the distribution for the state at 2.615 MeV is clearly more narrow suggesting $\ell = 0$ or $\ell = 1$.

The limits of the momentum axis represent the momentum acceptance (≈ 0.6 GeV/c) for this measurement. Depending on the width, each distribution may be truncated by the finite acceptance of the spectrograph. Therefore, branching ratios extracted in this measurement must include a correction to account for events that occur beyond the momentum acceptance window. This correction can only be roughly estimated due to difficulty in extracting distributions of sufficient quality for a number of the populated states. Losses beyond the acceptance window are estimated by linear extrapolation of the momentum distribution with a reasonable slope based on the shape of the distribution at the limit of acceptance. The estimated correction for the $\ell = 30.336$ MeV distribution is +15–20%, whereas a correction of +5–10% is found for most of the remaining distributions shown in Fig. 5. A negligible correction on the order of 1% is determined for the narrow 2.615-MeV distribution. Because these corrections are not well determined, they are not applied to the deduced branching ratios and serve as an estimate of additional systematic uncertainty.

Low-momentum tails that are not reproduced by calculations are apparent in all of the extracted distributions shown in Fig. 5. Although the origin of these tails is unknown, they are presumed to arise from dissipative processes already included in the momentum-integrated cross section [49]. Therefore, no corrections are applied to deduced knockout cross sections based on these tails, and fits to the extracted distributions include only momenta ranging from the low-momentum half-maximum point to the high-momentum acceptance limit.

B. Single-neutron knockout from ^{32}Mg

The inclusive cross section for single-neutron knockout from ^{32}Mg is determined to be 94(7) mb. The dominant part of this uncertainty arises from software cuts for the particle identification (7%). The larger uncertainty in the particle identification for the present measurement relative to that for the ^{30}Mg measurement results from an addition cut on the position in the focal plane required as a result of the larger momentum spread in the secondary beam. This

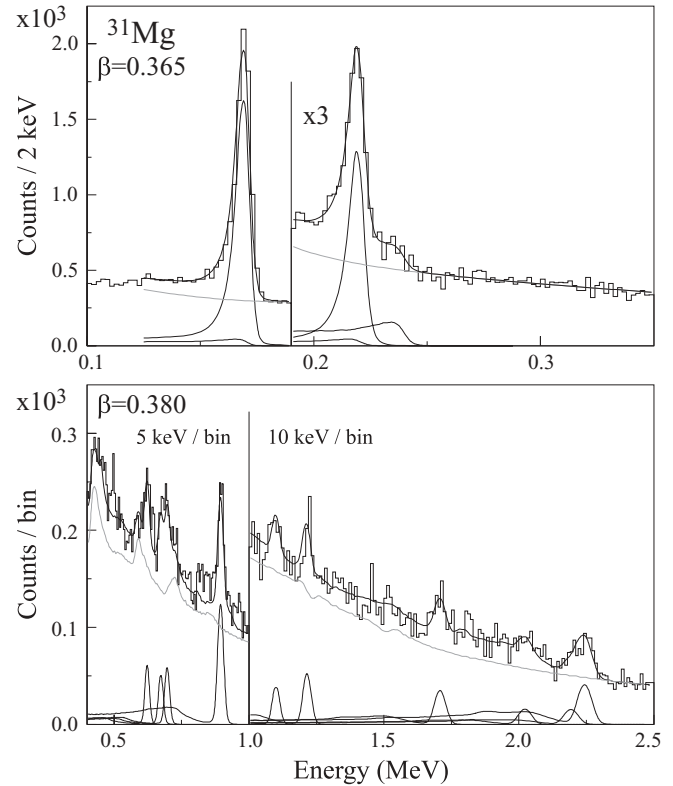


FIG. 6. γ -ray spectrum detected in coincidence with ^{31}Mg fragments. The upper panel shows the low-energy region of the spectrum that is Doppler reconstructed using a post-target fragment velocity. The lower panel shows the remainder of the analyzed spectrum, Doppler reconstructed using a midtarget fragment velocity. Results of statistical fits to each region of the spectrum are overlaid with individual photopeak response functions also plotted.

cross section includes acceptance correction only within the S800 acceptance but does not include corrections based on extrapolation beyond the acceptance window.

The Doppler-reconstructed γ -ray energy spectrum coincident with ^{31}Mg fragments is shown in Fig. 6. Two strong photopeaks are observed at 0.17 and 0.22 MeV with several more at higher energies. The two low-energy photopeaks are clearly skewed on the low-energy side due to the long lifetime of the 0.221-MeV state from which they are emitted. The half-life of this state has been measured to be 133(8) ps [50] which corresponds to a mean flight path of 1.5 cm for particles moving at approximately a third of the speed of light. Therefore, the low-energy region of the spectrum is Doppler reconstructed using the post-target beam velocity of 0.365c. With this reconstruction, a shoulder is observed in the spectrum on the high-energy side of the 0.221-MeV photopeak, which is consistent with the response of SeGA to a 0.240-MeV γ -ray emitted with a half-life on the order of nanoseconds. This transition originates from the excited state at 0.461 MeV with a known half-life of 10.5(8) ns [50] corresponding to a 1.2-m flight path. Therefore, a response function for the 0.240-MeV transition assuming the known half-life is also included in the analysis of the low-energy part of the spectrum. The remainder of the spectrum is Doppler reconstructed using a midtarget

TABLE III. Gamma-ray intensities and branching ratios for ^{31}Mg .

E_{level} (MeV)	E_{γ} (MeV)	I (%)	b (%)	σ (mb)
0.000			39.2(63)	36.8(68)
0.051				
0.221	0.221	6.50(45)	24.4(21)	22.9(26)
	0.171	19.1(12)		
0.461	0.240	22.1(58)	20.4(60)	19.1(58)
0.673	0.673	1.1(11)	2.9(18)	2.7(17)
	0.623	1.4(11)		
	0.452	0.0(10)		
0.945	0.895	4.8(11)	5.0(11)	4.7(11)
1.154	0.697	1.7(11)	1.7(11)	1.6(10)
2.244	2.244	3.82(79)	6.4(14)	6.0(13)
	2.193	1.38(78)		
	2.023	1.23(78)		
	1.100	1.1(10)		
	1.215	1.8(10)	Unplaced transitions	
	1.790	2.1(8)		

velocity of 0.380c, which is determined as discussed for the ^{30}Mg measurement.

The intensity of the 0.171-MeV photopeak is obtained from a fit to the spectrum ranging from 0.125 to 0.195 MeV. The fit includes a simulated response function assuming a 133-ps half-life as well as a second-order polynomial background. The 0.221- and 0.240-MeV photopeak intensities are obtained in a fit ranging from 0.178 to 0.400 MeV. This fit includes simulated response functions and a background modeled by the sum of two exponentials. Intensities are reported in Table III, which includes corrections of +3% and +6% for the 0.221-MeV and 0.171-MeV intensities, respectively, due to deviation of the simulated photopeak efficiency from the measured efficiency at 0.122 MeV.

The remainder of the spectrum is analyzed in two parts. The region from 0.4 to 1.0 MeV is analyzed at a resolution of 5 keV/bin, while the region from 1.0 to 2.5 MeV is analyzed at 10 keV/bin. Intensities are obtained from a fit to the spectrum, which includes simulated response functions, a reaction-correlated γ -ray continuum, and Doppler-broadened γ -ray transitions emitted from rest resulting from neutron interactions with the beam pipe and germanium detectors.

The shape of the background is modeled between 0.4 and 5.0 MeV by the sum of two exponentials and a constant and is fixed by a statistical fit to the γ -ray spectrum obtained in the single-neutron removal measurement from ^{28}Ne [13]. The $^9\text{Be}(^{28}\text{Ne},^{27}\text{Ne})\text{X}$ measurement was performed with the same setup as the present measurement, and no transition γ -rays were observed above 0.9 MeV. The fit to the 5 keV/bin region includes a free-varying exponential to correct the neon background; the correction becomes negligible for energies above 0.6–0.7 MeV.

Photopeaks at 0.62, 0.67, 0.69, and 0.90 MeV are observed in the 5 keV/bin region corresponding to previously observed γ -ray transitions [27,50]. Response functions for these and all other previously observed transitions are included in the

fit, yet only the clearly visible peaks have intensities greater than 0.5% of the inclusive cross section. In this region of the γ -ray spectrum, fluctuations in the residual of the fit suggest sensitivity to photopeaks with intensity of at least 1% of the inclusive cross section. Therefore, intensities below this level are considered consistent with zero, and a systematic uncertainty of 1% is added to all other intensities extracted in this region. The branching ratios for the depopulation of the state at 0.673 MeV is not well measured in the present results but is consistent with that reported in Ref. [27].

The 10 keV/bin region clearly includes photopeaks at 1.1, 1.2, 1.7, and 2.2 MeV. Transitions at 1.215, 2.244, and 2.193 MeV have been previously observed. However, the 1.1- and 1.7-MeV transitions have not. To confirm that these peaks are associated with ^{31}Mg , excited states were also populated by secondary fragmentation of ^{34}Si in a separate measurement using the same setup. From this data, new transitions at 1.100(5), 1.257(7), 1.506(5), 1.708(8), 1.790(5), and 1.945(7) MeV were established as belonging to ^{31}Mg but a placement in the level scheme was not possible. The new transitions and all previously known transitions in this energy region were included in the fit. However, several give intensities less than 0.5% of the inclusive cross section and are considered consistent with zero. Fluctuations in the fit residue are clearly more statistical in this region than in the 5 keV/bin region, but the reduced photopeak efficiency results in a minimum sensitivity ranging from approximately 0.5% at 1 MeV to 1% at 2.5 MeV. Branching ratios for the depopulation of the 2.244-MeV state are compared with those presented in Ref. [27], and a significant deviation is observed for the 1.215-MeV transition. According to Ref. [27] the intensity of the 1.215-MeV transition should be approximately 1/10th of the intensity of the 2.244 MeV transition. Further, the 1.215 should be accompanied by a subsequent 0.808-MeV transition that is not observed. Therefore, the 1.2-MeV peak must be a doublet with the majority of the intensity associated with a new unplaced transition.

Branching ratios are determined by intensity balancing of previously known and placed transitions, and results of this analysis are summarized in Table III. The entire intensity of the 1.2-MeV transition is listed as unplaced, whereas clearly some small part of it (0.4%, absolute) must be associated with population of the state at 2.244 MeV. However, according to the branching ratios reported in Ref. [27], this small part is well within the uncertainty of the total branch to the state at 2.244 MeV.

The longitudinal momentum distribution associated with the population of the state at 0.221 MeV is extracted by applying a combined gate on the 0.171- and 0.221-MeV photopeaks with background contributions subtracted as discussed for the ^{30}Mg measurement. The 0.221-MeV momentum distribution is shown in Fig. 7. The momentum acceptance of 0.5 GeV/c is reflected by the limits of the x axis, and acceptance losses are estimated for this distribution, as discussed for the ^{30}Mg measurement, to be approximately 1–2%. The gate for this distribution includes an approximate 6% contribution from the extended 0.240-MeV response functions, which should add a broad but negligible $\ell = 3$ component, and the γ -ray analysis suggests that 90% of the distribution is associated with direct

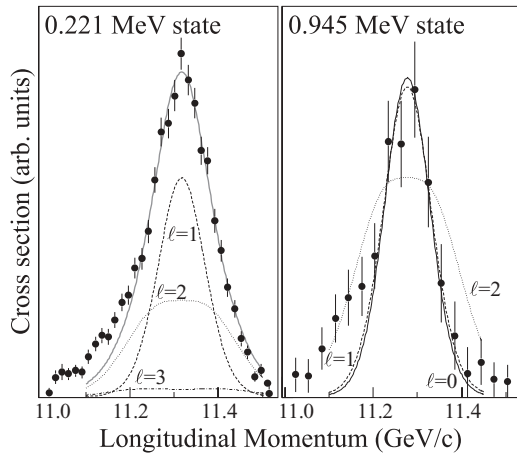


FIG. 7. Longitudinal momentum distributions for states populated in the knockout residue ^{31}Mg . The panel on the left shows the distribution associated with the population of the excited state at 0.221 MeV, whereas the right panel is that for the state at 0.945 MeV. The 0.945-MeV distribution is overlaid with calculated curves assuming $\ell = 0$ (solid), $\ell = 1$ (dashed), and $\ell = 2$ (dotted). The 0.221-MeV distribution is not reproduced by a single ℓ -value distribution likely due to indirect feeding. This distribution is fit with a combination of $\ell = 1$ and $\ell = 2$ with a fixed $\ell = 3$ component due to known contamination in the γ -ray energy gate.

feeding of the state at 0.221 MeV. However, the distribution is not reproduced by any single ℓ -value distribution. This leads to the conclusion that this state is populated indirectly by one or more unobserved or unplaced γ -ray transitions.

The 0.221-MeV distribution shown in Fig. 7 is overlaid with a fit that includes a narrow $\ell = 1$ and a broad $\ell = 2$ component as well as a small and fixed $\ell = 3$ component to model the 0.240-MeV contamination. The result of the fit suggests that the broad component accounts for 40(10)% of the cross section that feeds, either directly or indirectly, the state at 0.221 MeV or 10(3)% of the inclusive cross section. A fit was also performed in which the contamination is assumed to be purely $\ell = 3$ and the quoted estimate of the contamination is an average of the two results. No part of the contamination in this analysis is assumed to be $\ell = 0$ as this distribution is too similar to the $\ell = 1$ distribution. This presents a strong limitation to this analysis. The observed indirect feeding to the state at 0.221 MeV accounts for only 1.2(8)% of the inclusive cross section, leaving another 9(3)% of indirect feeding unobserved.

Three unplaced transitions with a total intensity of 4.9(16)% are observed in the γ spectrum and may feed the 0.221-MeV state. This scenario would explain the shape of the 0.221 MeV distribution assuming that all of these transitions are associated with broad momentum distributions ($\ell > 1$) and feed the state at 0.221 MeV. However, the possibility of indirect feeding from states populated with a branching ratio below the approximate 0.5–1% sensitivity cannot be excluded. It is important to note that this distribution is extracted by gating on a sharp photopeak resulting from prompt emission of a transition γ -ray. Therefore, feeding transitions contributing to this momentum distribution should also be prompt and

thus of good resolution, reducing the possible modes of nonobservation to (i) an intensity below the above mentioned sensitivity or (ii) an energy below the 0.1-MeV threshold.

The longitudinal momentum distribution for events populating the state at 0.945 MeV is also extracted by gating on the 0.895-MeV photopeak. Low statistics in this photopeak limit the quality of the extracted momentum distributions. However, this distribution is clearly narrow, indicating $\ell = 0$ or $\ell = 1$ and negligible acceptance losses. Given the limited statistics, it is not possible to extract a momentum distribution for other populated states. Acceptance corrections are calculated within the acceptance window as discussed for the ^{30}Mg measurement. Because momentum distributions are not available for a number of states in the present measurement, corrections due to momentum acceptance losses are estimated to be similar to those measured in the ^{30}Mg measurement for corresponding ℓ values. These systematic uncertainties are included in the discussion of the ^{32}Mg results.

IV. DISCUSSION

A. ^{30}Mg

The level structure of the ^{29}Mg knockout residue has been extensively investigated by means of fusion-evaporation reactions, multinucleon transfer, β decay, and β -delayed neutron decay [51]. The level structure of the knockout residue ^{29}Mg is compared to USD shell model calculations in Fig. 6 of Ref. [46]. Present results are consistent with this interpretation of the level scheme. In particular, spin and parity assignments for the states at 2.500 and 2.615 MeV are supported by the respective broad and narrow momentum distributions observed for these states. Although no direct feeding is observed to excited states at 1.095 and 1.431 MeV in β decay from the positive-parity ^{29}Na ground state, they are populated in the β - n reaction from ^{30}Na , suggesting a negative parity assignment [46,47]. Cross sections to these states in the $^{30}\text{Si}(^{13}\text{C}, ^{14}\text{O})^{29}\text{Mg}$ reactions are approximately equal to those for the population of the first $3/2^-$ and $7/2^-$ states of ^{27}Mg in the $^{28}\text{Si}(^{13}\text{C}, ^{14}\text{O})^{27}\text{Mg}$ reaction [52], suggesting assignments of $3/2^-$ and $7/2^-$ for the respective states at 1.095 and 1.431 MeV. Momentum distributions observed for these two states in the present measurement (see Fig. 5) support this assignment.

Cross sections for the single-neutron knockout from ^{30}Mg are compared to shell-model calculations in Table IV. Single-particle cross sections σ_{sp} for single-neutron removal are calculated in a three-body eikonal reaction model [33,34]. Deduced spectroscopic factors $C^2 S_{\text{exp}}$ are given as the ratio of the measured partial cross sections to the corresponding calculated single-particle cross sections. The deduced spectroscopic factors carry an additional systematic uncertainty due to momentum acceptance losses as discussed in Sec. III A. Predicted spectroscopic factors and single-particle occupancies obtained from an OXBASH [53] calculation using the USD interaction [22] are included as well as single-particle occupancies obtained from a Monte Carlo shell-model calculation [21] using the SDPF-M interaction [54]. As indicated in Fig. 2 and shown in Table IV, USD and SDPF-M single-particle occupancies are in good agreement for the ^{30}Mg ground state

TABLE IV. Deduced spectroscopic strengths and calculated single-particle occupancies for ^{30}Mg . With the exception of ℓ values given for the ground state doublet, the listed ℓ values indicate values or constraints deduced in the present work. Values given for the ground state doublet are assumed based on spin and parity assignments from previous measurements.

E_{level} (MeV)	ℓ	σ_{exp} (mb)	σ_{sp} (mb)	C^2S_{exp}	C^2S_{USD}	$n\ell j$	$\langle n \rangle_{\text{USD}}$	$\langle n \rangle_{\text{SDPF-M}}$
0.000	(2)	47.4(38)	17.9		1.31	$1d_{3/2}$	2.27	1.82
0.055	(0)		25.3		1.46	$2s_{1/2}$	1.90	1.81
1.095	1	4.3(15)	22.8	0.19(7)		$2p_{3/2}$	–	0.08
1.431	3	6.7(17)	16.4	0.41(10)		$1f_{7/2}$	–	0.52
1.642	2	7.3(15)	16.0	0.46(9)	0.20	$1d_{5/2}$	5.83	5.77
2.500	(2,3)	3.7(15)	16.1	0.23(9)	0.23			
2.615	(0,1)	6.9(15)	20.5	0.34(7)	0.22			
3.232	2	21.5(22)	15.5	1.39(14)	1.76 ^a			
3.674		2.3(10)						

^aSummed C^2S_{USD} for 3/2 and 5/2 states predicted at 3.23 and 3.04 MeV.

with the exception of a modest occupancy in fp single-particle states included in the latter. Further, USD spectroscopic factors predict strong feeding to the $3/2^+$ ground state, the low-lying $1/2^+$ excited state, and two $5/2^+$ excited states near the neutron-separation energy. Observed partial cross sections are in qualitative agreement with this prediction showing strong feeding of the ground state and low-lying first excited state and a doublet of states with $\ell = 2$ near the neutron threshold.

Although the results of this measurement on ^{30}Mg are in qualitative agreement with USD shell-model predictions, indicating the dominance of $0p-0h$ configurations in the ground state, significant spectroscopic strength is observed to the low-lying negative-parity states at 1.095 and 1.431 MeV, as shown in Table IV. Although spectroscopic factors are not yet available from MCSM calculations, the observed spectroscopic strength is compared to upper limits provided by the SDPF-M-calculated total occupancy in each single-particle state. The predicted occupancy in the $\nu 2p_{3/2}$ orbital is rather small at 0.081 neutrons. The observed spectroscopic strength in the lowest $3/2^-$ state is already more than twice the predicted full occupancy of the corresponding single-particle state, revealing a significant deviation from SDPF-M calculations. The observed $7/2^-$ spectroscopic strength is less than the SDPF-M upper limit, accounting for 80(20)% of the calculated $\nu 1f_{7/2}$ occupancy.

The observed spectroscopic strength to the lowest two negative-parity states appears to be consistent with single-particle occupancies calculated with the SDPF-M interaction. However, there is an additional negative-parity state suggested at 2.266 MeV based on β -delayed neutron emission measurements [47]. In the present experiment, significant direct feeding to a state at 2.28 MeV is observed. Although this state is not definitely identified as that observed at 2.266 MeV in Ref. [47], this possibility is not excluded. The momentum distribution for the state at 2.28 MeV is not well extracted (and not shown in Fig. 5) making a definitive ℓ -value assignment impossible. However, the width of the distribution makes $\ell = 3$ unlikely. Therefore, if this state is found to be a negative-parity state, then the present work indicates a spin constraint of $(1/2, 3/2)$; the former perhaps indicating the influence of the

$2p_{1/2}$ single-particle state, which is outside of the SDPF-M model space, and the latter suggesting a more significant underestimation of the total $2p_{3/2}$ occupancy in the ground state of ^{30}Mg .

B. ^{32}Mg

The level scheme of ^{31}Mg below 0.5 MeV based on previous experiments is shown in Fig. 8. The ground-state spin and parity have been determined to be $1/2^+$ [11]. Results from β decay and β -delayed neutron measurements suggest positive parity for the two lowest states and negative parity for the states at 0.221 and 0.240 MeV [27]. Measured lifetimes of the states at 0.221- and 0.461-MeV excited states [50] and the state at 0.051 MeV [27] limit multiplicities to dipole for the lower three transitions and quadrupole for the 0.240-MeV transition. These results compare well with shell-model predictions [27,50] that include particle-hole excitations across the $N = 20$ shell gap, motivating the given tentative assignments. Although these tentative assignments cannot be confirmed in the present analysis, they are adopted in discussing results.

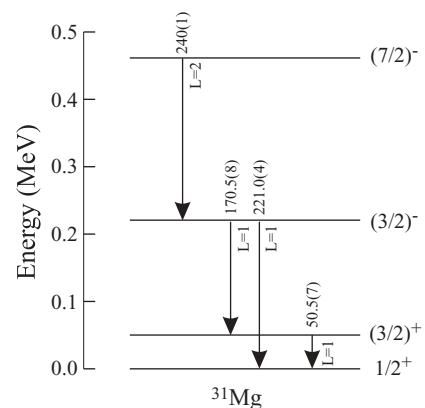


FIG. 8. Observed level scheme for ^{31}Mg . The L represent multipole orders deduced by lifetime measurements.

TABLE V. Deduced spectroscopic factors and calculated single-particle occupancies for ^{32}Mg . The ℓ values given in parentheses are assumed based on previous measurements.

E_{level} (MeV)	ℓ	σ_{exp} (mb)	σ_{sp} (mb)	C^2S_{exp}	$n\ell j$	$(n)_{\text{SDPF-M}}$
0.000	(0)	36.8(68)	25.9		$2s_{1/2}$	1.90
0.051	(2)		17.4		$1d_{3/2}$	2.12
0.221	(1)	15.4(28)	26.3	0.59(11)	$2p_{3/2}$	0.32
0.461	(3)	19.1(58)	16.0	1.19(36)	$1f_{7/2}$	1.83
0.673		2.7(17)			$1d_{5/2}$	5.83
0.945		4.7(11)				
1.154		1.6(10)				
2.244		6.0(13)				

The present measurement reveals strong feeding of the first two negative-parity states in ^{31}Mg by the single-neutron knockout reaction. The observed spectroscopic strengths to the low-lying $3/2^-$ and $7/2^-$ states are listed in Table V but carry an additional systematic uncertainty as discussed in Sec. III B. The $7/2^-$ spectroscopic strength is assumed to include no unobserved indirect feeding and is consistent with the predicted SDPF-M upper limit accounting for 65(20)% of the SDPF-M predicted full occupancy. The quoted $3/2^-$ strength represents an upper limit extracted by a combination of γ -ray analysis and a fit to the momentum distribution. From the γ -ray analysis the fraction of the inclusive cross section that feeds, both directly and indirectly, the state at 0.221 MeV is obtained. From the fit to the momentum distribution, 60(10)% of the cross section is attributed to $\ell = 0, 1$ states. The quoted $3/2^-$ spectroscopic strength exceeds the SDPF-M upper limit by nearly a factor of 2, suggesting a possible systematic underprediction of the $1p_{3/2}$ occupancy in SDPF-M calculations. However, systematic uncertainties in the $3/2^-$ spectroscopic factor must be considered.

The upper limit of the $3/2^-$ spectroscopic factor is obtained by assuming negligible $\ell = 0$ indirect feeding to the low-lying state at 0.221 MeV. To assess the validity of this assumption, it is noted that the ^{32}Mg ground state is well reproduced, assuming a pure 2p-2h excitation across the $N = 20$ shell gap [10]. The observed large spectroscopic factor to the low-lying $7/2^-$ state alone suggests the importance of particle-hole configurations across the $N = 20$ gap in the ground state of ^{32}Mg . In the present discussion we assume that the ^{32}Mg ground state can be treated as a pair of neutrons in the fp shell coupled to the ^{30}Mg ground state such that spectroscopic strength to positive-parity states (sd model space) should compare well with those measured for the ^{30}Mg ground state. In fact, population of the ground state and/or the low-lying first excited state accounts for most of the positive-parity feeding, similar to the ^{30}Mg measurement. In contrast to the ^{30}Mg measurement, significant population of higher excited states is not observed in the present measurement. However, with the low neutron separation energy of $S_n = 2.378(15)$ MeV [55], the suggested higher-lying strength may fall beyond the neutron threshold, and overall results are consistent with the above-mentioned assumption for the structure of the ^{32}Mg ground state.

The actual extent of $\ell = 0$ indirect feeding into the state at 0.221 MeV cannot be determined. Consequently, the deduced $3/2^-$ spectroscopic factor carries a systematic uncertainty. Based on the simple assumption for the ^{32}Mg ground-state structure, the systematic uncertainty is approximated by the $\ell = 0$ spectroscopic strength of 0.34(7) observed in the high-energy level scheme of ^{29}Mg in the ^{30}Mg single-neutron knockout measurement. It is noted that if this spectroscopic strength is observed in ^{31}Mg , the cross section to the corresponding $1/2^+$ state must be approximately 6 mb, which agrees quite well with the cross section observed to the state at 2.244 MeV in ^{31}Mg . The observed branch of this state to the 0.211 MeV states is only 20%, giving a correction of -0.07 to the deduced $3/2^-$ spectroscopic factor. Although no further evidence exists to support a $1/2^+$ assignment to the ^{31}Mg state at 2.244 MeV, this discussion illustrates that the quoted systematic uncertainty in the $3/2^-$ spectroscopic strength is likely overestimated because decay from a higher-lying $1/2^+$ state to the ground-state doublet would be energetically favored.

C. Transition into the island of inversion

The summed negative-parity spectroscopic strength of 0.60(12) and 1.78(38) deduced for ^{30}Mg and ^{32}Mg , respectively, represents a direct observation of at least this many neutrons occupying fp single-particle states. The latter value is an upper limit because indirect feeding cannot be excluded in the deduced cross sections. Because spectroscopic strength is often concentrated in the lowest-lying excited states of given spin and parity, this sum is taken as a good estimate of the total fp occupancy. These results suggest a dramatic increase in fp single-particle occupancy by a factor of approximately 3 between ^{30}Mg and ^{32}Mg .

A comparison of deduced negative-parity spectroscopic factors to SDPF-M-calculated single-particle occupancies for $^{30,32}\text{Mg}$ is shown in Fig. 9. As shown in the right panel,

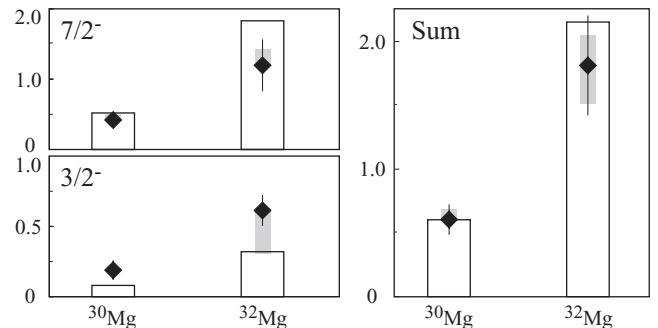


FIG. 9. Comparison of deduced spectroscopic factors to SDPF-M single-particle occupancies. Deduced spectroscopic factors are indicated by data points with systematic uncertainties shown as gray bars. SDPF-M occupancies are represented by bars. The left panels show a comparison of deduced spectroscopic factors to the lowest $7/2^-$ and $3/2^-$ states to the respective SDPF-M calculated $0f_{7/2}$ and $1p_{3/2}$ occupancies. The panel on the right shows a comparison of the sum of these deduced spectroscopic strengths to the summed fp SDPF-M single-particle occupancy.

the summed negative-parity spectroscopic strength compares well with fp single-particle occupancies obtained using the SDPF-M interaction [23,24]. These results provide a first *direct* observation of a $N = 20$ cross-shell intruder admixture in the ground state of $^{30,32}\text{Mg}$. Further, present results provide a first observation of intruder admixtures in the ground state of ^{30}Mg , providing an important test of the understanding of the weakening $N = 20$ shell gap. Quantitative agreement with SDPF-M calculations for ^{30}Mg indicate an accurate treatment of the transition from normal to intruder dominance in the ground states of magnesium isotopes.

V. SUMMARY

Single-neutron knockout measurements have been performed from $^{30,32}\text{Mg}$ revealing significant direct population of negative-parity states in the $^{29,31}\text{Mg}$ knockout residues. Population of negative-parity states in this reaction gives direct and quantitative evidence of the presence of $N = 20$ cross-shell intruder configurations in the ground states of $^{30,32}\text{Mg}$. With J^π assignments supported by analysis of extracted longitudinal momentum distributions for excited states at 1.095 and 1.431 MeV in ^{29}Mg and by a number of previous observations for states at 0.221 and 0.461 MeV in ^{31}Mg , spectroscopic factors are extracted that quantify the extent

of these intruder admixtures. Deduced spectroscopic factors from the present measurements are compared to SDPF-M calculated single-particle occupancies, which provide occupation numbers and thus an upper limit for the spectroscopic strengths. Although the deduced $7/2^-$ spectroscopic strengths compare well with SDPF-M calculations, $3/2^-$ spectroscopic strengths are underpredicted by at least a factor of 2. The total observed spectroscopic strength to negative-parity states for ^{30}Mg is 0.60(12), whereas, for ^{32}Mg , it is three times as large at 1.78(38), indicating a dramatic shift in structure with the addition of two neutrons. This sudden increase in fp occupancy is in good agreement with SDPF-M calculations, illustrating the predictive power of the interaction in this region.

ACKNOWLEDGMENTS

This work is supported by the United States National Science Foundation under contracts PHY-0606007 and PHY-0555366, by the UK Engineering and Physical Sciences Research Council (EPSRC) under grant no. EP/D003628, by a Grant-in-Aid for Specially Promoted Research (13002001) and a Grant-in-Aid for Young Scientists (14740176) from the MEXT, by the RIKEN-CNS collaboration project on large-scale nuclear structure calculation, and by the JSPS core-to-core project, EFES.

-
- [1] C. Thibault, R. Klapisch, C. Rigaud, A. M. Poskanzer, R. Prieels, L. Lessard, and W. Reisdorf, *Phys. Rev. C* **12**, 644 (1975).
- [2] T. Glasmacher, *Annu. Rev. Nucl. Part. Sci.* **48**, 1 (1998).
- [3] Y. Yanagisawa, M. Notani, H. Sakurai, M. Kunibu, H. Akiyoshi, N. Aoi, H. Baba, K. Demichi, N. Fukuda, H. Hasegawa *et al.*, *Nucl. Phys.* **A734**, 374 (2004).
- [4] H. Iwasaki, T. Motobayashi, H. Sakurai, K. Yoneda, T. Gomi, N. Aoi, N. Fukuda, Z. Fülöp, U. Futakami, Z. Gacsi *et al.*, *Phys. Lett.* **B522**, 227 (2001).
- [5] B. V. Pritychenko, T. Glasmacher, P. D. Cottle, M. Fauerbach, R. W. Ibbotson, K. W. Kemper, V. Maddalena, A. Navin, R. Ronningen, A. Sakharuk *et al.*, *Phys. Lett.* **B461**, 322 (1999).
- [6] B. V. Pritychenko, T. Glasmacher, B. A. Brown, P. D. Cottle, R. W. Ibbotson, K. W. Kemper, L. A. Riley, and H. Scheit, *Phys. Rev. C* **63**, 011305(R) (2000).
- [7] B. V. Pritychenko, T. Glasmacher, P. D. Cottle, R. W. Ibbotson, K. W. Kemper, L. A. Riley, A. Sakharuk, H. Scheit, M. Steiner, and V. Zelevinsky, *Phys. Rev. C* **65**, 061304(R) (2002).
- [8] K. Yoneda, H. Sakurai, T. Gomi, T. Motobayashi, N. Aoi, N. Fukuda, U. Futakami, Z. Gacsi, Y. Higurashi, N. Imai *et al.*, *Phys. Lett.* **B499**, 233 (2001).
- [9] J. A. Church, C. M. Campbell, D.-C. Dinca, J. Enders, A. Gade, T. Glasmacher, Z. Hu, R. V. F. Janssens, W. F. Mueller, H. Olliver *et al.*, *Phys. Rev. C* **72**, 054320 (2005).
- [10] E. K. Warburton, J. A. Becker, and B. A. Brown, *Phys. Rev. C* **41**, 1147 (1990).
- [11] G. Neyens, M. Kowalska, D. Yordanov, K. Blaum, P. Himpe, P. Lievens, S. Mallion, R. Neugart, N. Vermeulen, Y. Utsuno *et al.*, *Phys. Rev. Lett.* **94**, 022501 (2005).
- [12] V. Tripathi, S. L. Tabor, P. F. Mantica, C. R. Hoffman, M. Wiedeking, A. D. Davies, S. N. Liddick, W. F. Mueller, T. Otsuka, A. Stolz *et al.*, *Phys. Rev. Lett.* **94**, 162501 (2005).
- [13] J. R. Terry, D. Bazin, B. A. Brown, C. M. Campbell, J. A. Church, J. M. Cook, A. D. Davies, D.-C. Dinca, J. Enders, A. Gade *et al.*, *Phys. Lett.* **B640**, 86 (2006).
- [14] A. Gade, P. Adrich, D. Bazin, M. D. Bowen, B. A. Brown, C. M. Campbell, J. M. Cook, S. Ettenauer, T. Glasmacher, K. W. Kemper *et al.*, *Phys. Rev. Lett.* **99**, 072502 (2007).
- [15] B. A. Brown, *Prog. Part. Nucl. Phys.* **47**, 517 (2001).
- [16] A. Navin, D. W. Anthony, T. Aumann, T. Baumann, D. Bazin, Y. Blumenfeld, B. A. Brown, T. Glasmacher, P. G. Hansen, R. W. Ibbotson *et al.*, *Phys. Rev. Lett.* **85**, 266 (2000).
- [17] S. D. Pain, W. N. Catford, N. A. Orr, J. C. Angélique, N. I. Ashwood, V. Bouchat, N. M. Clarke, N. Curtis, M. Freer, B. R. Fulton *et al.*, *Phys. Rev. Lett.* **96**, 032502 (2006).
- [18] T. Otsuka, R. Fujimoto, Y. Utsuno, B. A. Brown, M. Honma, and T. Mizusaki, *Phys. Rev. Lett.* **87**, 082502 (2001).
- [19] T. Otsuka, T. Suzuki, R. Fujimoto, H. Grawe, and Y. Akaishi, *Phys. Rev. Lett.* **95**, 232502 (2005).
- [20] T. Otsuka, Y. Utsuno, M. Honma, and T. Mizusaki, *Prog. Part. Nucl. Phys.* **46**, 155 (2001).
- [21] T. Otsuka, M. Honma, T. Mizusaki, N. Shimizu, and Y. Utsuno, *Prog. Part. Nucl. Phys.* **47**, 319 (2001).
- [22] B. H. Wildenthal, *Prog. Part. Nucl. Phys.* **11**, 5 (1984).
- [23] Y. Utsuno, T. Otsuka, T. Glasmacher, T. Mizusaki, and M. Honma, *Phys. Rev. C* **70**, 044307 (2004).
- [24] Y. Utsuno, T. Otsuka, T. Mizusaki, and M. Honma, *Phys. Rev. C* **60**, 054315 (1999).
- [25] O. Niedermaier, H. Scheit, V. Bildstein, H. Boie, J. Fitting, R. von Hahn, F. Köck, M. Lauer, U. K. Pal, H. Podlech *et al.*, *Phys. Rev. Lett.* **94**, 172501 (2005).
- [26] F. Maréchal, D. L. Balabanski, D. Borremans, J.-M. Daugas, F. de Oliveira Santos, P. Dessagne, G. Georgiev, J. Giovinazzo, S. Grévy, P. Himpe *et al.*, *Phys. Rev. C* **72**, 044314 (2005).

- [27] G. Klotz, P. Baumann, M. Bounajma, A. Huck, A. Knipper, G. Walter, G. Marguier, C. Richard-Serre, A. Poves, and J. Retamosa, *Phys. Rev. C* **47**, 2502 (1993).
- [28] H. Iwasaki, T. Motobayashi, H. Sakurai, K. Yoneda, T. Gomi, N. Aoi, N. Fukuda, Z. Fülöp, U. Futakami, Z. Gacsi *et al.*, *Phys. Lett.* **B620**, 118 (2005).
- [29] A. Obertelli, A. Gillibert, N. Alamanos, M. Alvarez, F. Auger, R. Dayras, A. Drouart, G. de France, B. Jurado, N. Keeley *et al.*, *Phys. Lett.* **B633**, 33 (2006).
- [30] Z. Dombrádi, Z. Elekes, A. Saito, N. Aoi, H. Baba, K. Demichi, Z. Fülöp, J. Gibelin, T. Gomi, H. Hasegawa *et al.*, *Phys. Rev. Lett.* **96**, 182501 (2006).
- [31] P. G. Hansen and J. A. Tostevin, *Annu. Rev. Nucl. Part. Sci.* **53**, 219 (2003).
- [32] B. A. Brown, P. G. Hansen, B. M. Sherrill, and J. A. Tostevin, *Phys. Rev. C* **65**, 061601(R) (2002).
- [33] J. A. Tostevin, *Nucl. Phys.* **A682**, 320c (2001).
- [34] J. A. Tostevin, *J. Phys. G* **25**, 735 (1999).
- [35] P. G. Hansen, *Phys. Rev. Lett.* **77**, 1016 (1996).
- [36] C. A. Bertulani and P. G. Hansen, *Phys. Rev. C* **70**, 034609 (2004).
- [37] C. A. Bertulani and A. Gade, *Comput. Phys. Commun.* **175**, 372 (2006).
- [38] P. S. Miller, F. Marti, D. Poe, M. Steiner, J. Stetson, A. Stolz, and P. Zavodszky, in *Proceedings of the 17th International Conference on Cyclotrons and Their Applications*, edited by A. Goto and Y. Yano (Particle Accelerator Society of Japan, Tokyo, Japan, 2005), p. 62.
- [39] D. J. Morrissey, B. M. Sherrill, M. Steiner, A. Stolz, and I. Wiedenhoever, *Nucl. Instrum. Methods B* **204**, 90 (2003).
- [40] D. Bazin, J. A. Caggiano, B. M. Sherrill, J. Yurkon, and A. Zeller, *Nucl. Instrum. Methods B* **204**, 629 (2003).
- [41] J. Yurkon, D. Bazin, W. Benenson, D. J. Morrissey, B. M. Sherrill, D. Swan, and R. Swanson, *Nucl. Instrum. Methods A* **422**, 291 (1999).
- [42] W. F. Mueller, J. A. Church, T. Glasmacher, D. Gutknecht, G. Hackman, P. G. Hansen, Z. Hu, K. L. Miller, and P. Quirin, *Nucl. Instrum. Methods A* **466**, 492 (2001).
- [43] G. Scheidenberger and H. Geissel, *Nucl. Instrum. Methods B* **135**, 25 (1998).
- [44] <http://www-linux.gsi.de/~weick/atima/>
- [45] D. Bazin, O. Tarasov, M. Lewitowicz, and O. Sorlin, *Nucl. Instrum. Methods A* **482**, 307 (2002).
- [46] P. Baumann, P. Dessagne, A. Huck, G. Klotz, A. Knipper, G. Marguier, C. Miehe, M. Ramdane, C. Richard-Serre, G. Walter *et al.*, *Phys. Rev. C* **36**, 765 (1987).
- [47] P. Baumann, P. Dessagne, A. Huck, G. Klotz, A. Knipper, C. Miehe, M. Ramdane, G. Walter, G. Marguier, H. Gabelmann *et al.*, *Phys. Rev. C* **39**, 626 (1989).
- [48] M. Berz, K. Joh, J. A. Nolen, B. M. Sherrill, and A. F. Zeller, *Phys. Rev. C* **47**, 537 (1993).
- [49] A. Gade, D. Bazin, C. A. Bertulani, B. A. Brown, C. M. Campbell, J. A. Church, D.-C. Dinca, J. Enders, T. Glasmacher, P. G. Hansen *et al.*, *Phys. Rev. C* **71**, 051301(R) (2005).
- [50] H. Mach, L. M. Fraile, O. Tengblad, R. Boutami, C. Jollet, W. A. Plóciennik, D. T. Yordanov, M. Stanoiu, M. J. G. Borge, P. A. Butler *et al.*, *Eur. Phys. J. A* **25**, s01, 105 (2005).
- [51] P. M. Endt, *Nucl. Phys.* **A521**, 1 (1990).
- [52] C. L. Woods, W. N. Catford, L. K. Fifield, N. A. Orr, and R. J. Sadleir, *Nucl. Phys.* **A476**, 392 (1988).
- [53] B. A. Brown, A. Etchegoyen, and W. D. M. Rae, *Tech. Rep. 524*, Michigan State University Cyclotron Lab (1988).
- [54] Y. Utsuno, T. Otsuka, T. Mizusaki, and M. Honma, *Phys. Rev. C* **64**, 011301(R) (2001).
- [55] G. Audi, A. H. Wapstra, and C. Thibault, *Nucl. Phys.* **A729**, 337 (2003).